Three-Dimensional Characterization of Incipiently Spalled Tantalum

J. F. BINGERT, B. L. HENRIE, and D.L. WORTHINGTON

Three-dimensional (3-D) characterization techniques have been applied to quantitatively assess shock-induced damage in an incipiently spalled tantalum plate. A significant sample volume was imaged and volumetrically reconstructed *via* serial sectioning techniques. An analysis of segmented void damage revealed distributions regarding void size, morphology, spatial variations, and nearest-neighbor distances (NNDs). The latter two distributions highlight the necessity of 3-D data sets to capture the feature statistics. Very limited correlation was observed between void size and clustering tendency. Electron backscatter diffraction (EBSD) was applied to investigate spatial relationships between the damage features and the relative levels of induced plasticity. Large variations in microstructural character were found between different intervoid regions, independent of ligament width. The use of intragranular misorientation deviation (IMD) maps in two and three dimensions reveals surprisingly contiguous and complex plastic linkages not obviously predicted from the void-dominated damage field. Overall, 3-D characterization of shock-damaged material is shown to provide statistics and insight regarding the true damage field unobtainable from two-dimensional (2-D) data sets, and will provide meaningfully improved data for predictive damage models.

I. INTRODUCTION

THE ductile dynamic failure, or spall, of metals occurs through a sequential process of nucleation, growth, and coalescence of voids and cracks that initiate at the microstructural scale. Spall refers to the damage and failure process produced by tensile release, or rarefaction, waves associated with shock-induced deformation. The spallation process is affected by shock parameters such as pressure, pulse duration, and pulse shape, along with material variables that include constitutive properties, microstructure, and anisotropy. There exists a sympathetic response between the stress state that initiates damage and the plastic response to that stress state. For example, the plastic zone surrounding a void may be influenced by both the applied stress and the stress field associated with the void. Spall damage broadly occurs in two modes: cavitation voids induced by hydrostatic tensile stresses, and shear localizations and cracks that form microstructural damage links between voids. Incipient spallation results if spall processes do not produce a complete separation of material; that describes the condition of the sample characterized in the present work.

The evolution of damage and the effect of microstructural and stress-state variables on this evolution have been the subject of several previous studies, *e.g.*, References 1 through 11. A description of the true damage field is an important component of understanding the mechanisms controlling the failure process and estimating the relative effect of shock and microstructural variables on this process; it also serves as a source to both inform and validate dynamic damage models.[12–14] Historically, the damage quantification related to spalled materials has been determined by the stereological analysis of two-dimensional (2-D) metallographic sections.[2] This stereologic approach assumes that a representative section or sections are quantified. If the features of interest are distributed heterogeneously in the material, then the number of sections required for statistical robustness increases. However, a 2-D section cannot fully describe arbitrary shapes, and, more significantly, cannot reproduce the true relationship between damage features. Three-dimensional (3-D) characterization is necessary to establish these linkages with certitude.

The motivation behind the current work is, therefore, to characterize and quantify the true damage network in a spalled tantalum sample, in order to provide realistic input for improved damage models. Toward this goal, the effect of microstructure and shock parameters on incipient spall and the interaction between damage and microstructure were investigated. The approach is to distill structure-property information in order to link details of the microstructure to damage evolution. Tantalum is a representative ductile bcc metal, and the plate examined in this study has an extensive pedigree.[15] Of particular interest was the spatial

J.F. BINGERT, Technical Staff Member, is with the Materials Science and Technology Division, Los Alamos National Laboratory, Los Alamos, NM 87545. B.L. HENRIE, Technical Staff Member, formerly with the Materials Science and Technology Division, Los Alamos National Laboratory, is Project Manager, Stanley Associates, Inc., Huntsville, AL 35805, USA. D.L. WORTHINGTON, Student, is with the Department of Mechanical Engineering, University of California, Davis, CA 95616 and the Materials Design Institute, Los Alamos National Laboratory. Contact e-mail: bingert@lanl.gov
Manuscript submitted June 23, 2006.
Article published online July 7, 2007.

distribution of the nearest-neighbor voids, since this provides an indication of preferred initiation site density and distribution.

Three-dimensional microstructural characterization is rapidly gaining acceptance as a powerful means to explore microstructural relationships,[16–25] especially those that lead to an improved understanding of the mechanisms and kinetics behind their formation. For example, 3-D characterization of ductile damage at quasi-static rates has been performed by X-ray tomographic techniques,[26–28] but the limited resolution and poor penetration capabilities for high-Z metals, such as tantalum, precluded its application in the present study. The application of 3-D reconstruction techniques of any kind to the investigation of spall damage has not been undertaken to date, as far as the authors know. In this study, a spalled tantalum sample was three-dimensionally characterized to ascertain important statistical information regarding the damage network and its relationship to the parent structure.

II. EXPERIMENTAL/COMPUTATIONAL DETAILS

The baseline material consisted of a 10-mm-thick rolled tantalum plate in the as-received, annealed condition. The plate composition was high purity, with O, N, C, and H contents < 50, 10, 10, and 5 ppm, respectively. Other detectable impurities were below the resolution limits of 5 ppm, or 25 ppm in the case of W and Nb. Consistent with the low impurity levels, neither precipitates nor inclusions were observed in the baseline microstructure, nor were any observed within several analyzed voids. The average grain size was 42 μm, as measured by optical microscopy-based stereology methods, and 33 μm as measured by crystallographic orientation data acquired by electron backscatter diffraction (EBSD) characterization. Other aspects of the microstructure have been previously characterized and are reported elsewhere.[15,19]

For an overview of the general spall-testing experimental technique, see Meyers.[30] The schematics shown in Figure 1 reveal how the reconstructed sample volume relates to the spall experiment. Figure 1(a) shows a distance-time plot representing the spall experimental conditions (adapted from Meyers[1]), while Figure 1(b) shows a schematic of the subject incipient spallation sample with its frame of reference consistent with that from the experimental reference frame in Figure 1(a). The x-direction represents the spall sample radial direction, while y is the through-thickness direction in the plate, which is parallel to the impact direction. The spall plane is contained in the xz sample plane. A 4.06-mm-thick by 18-mm-diameter sample sectioned from the plate was incipiently spalled using a plate-on-plate impact geometry. An 80-mm single-stage gas gun was used to perform the shock experiment, with a 2.08-mm-thick flyer plate designed to impact the sample. The impact velocity was 199 ms^{-1}, and the peak pressure as determined by velocity interferometer system for any reflector (VISAR) diagnostics was 5.6 GPa. Important to note are the absolute dimensions and the ratio of flyer thickness to target thickness. For this
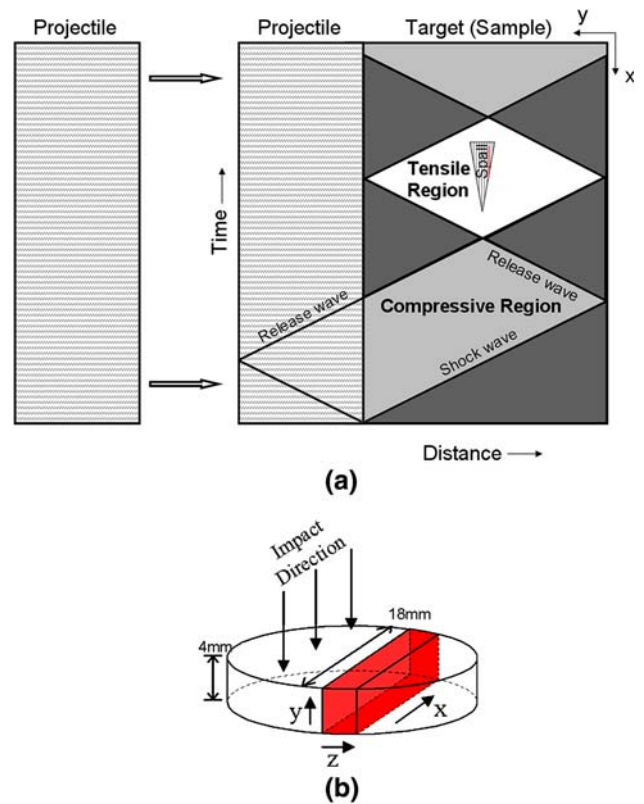

(a)

(b)

Fig. 1—Schematics representing the spall experimental conditions, showing (a) a distance-time plot (adapted from Meyers[1]) indicating shock wave propagation, nominal stress-state zones, and the spall sample reference frame and (b) the subject incipient spall shock sample with the characterized volume and sample frame of reference indicated with respect to the experimental reference frame in (a).

case, the dimensions resulted in a pulse duration of 1.1 μs, and the flyer/target ratio of 0.5 produced a principal spall plane that nominally resides at the midthickness of the sample. A related tantalum sample with twice the thickness of flyer plate and target was also tested, resulting in equivalent spall conditions, except for twice the pulse duration (2.2 μs). A comparison of the two samples to determine the effect of the pulse duration on the damage field is the subject of ongoing research.

A 7-mm-thick (z-direction) section of the shocked Ta disc was removed from the center of the plate. This section was mounted with epoxy on an aluminum fixture. In this configuration, the xy plane was the plane of observation, while the serial section material removal was along the z direction. The specimen fixture allowed for transfer between the polisher, optical microscope, and scanning electron microscope (SEM) without detaching the specimen. Polishing was performed on an Allied Multiprep polisher (Allied High Tech Products, Inc., Rancho Dominguez, California 90220). A six-step procedure was developed to remove ~5 μm of material between each serial section. Mechanical polishing was performed in the following sequence: 5-, 3-, and 1-μm alumina lapping film, followed by colloidal silica. After mechanical polishing, the sample was chemically polished for 3 minutes with a solution of 25 mL lactic acid, 10 mL nitric acid, and 5 mL hydrofluoric acid.[31] Etching was performed for 25 seconds

with a solution of 20 mL nitric acid, 20 mL hydrofluoric acid, and 60 mL sulfuric acid. Before serial sectioning was undertaken, it was verified that this procedure did not result in growth of the voids, as compared to the as-polished condition. The chemical polish and etch may be expected to smooth the internal void surface at the microscale, but this will not significantly alter the void dimension in subsequent sections.

Light optical micrograph montages of the sample xy cross section were taken on an Axiophot Zeiss microscope (Carl Zeiss MicroImaging, Inc., Thornwood, NY 10594) with Olympus Discover software (Olympus America Inc., Center Valley, PA 18034) at 50× and 100× magnifications for each serial section on the polished and etched surfaces. A 50× montage of 18 frames was required to capture the complete damage field that incorporated all of the voids from the xy section plane. The 50× montage covered an area 15.75 × 3.9 mm and yielded a resolution of 1.36 μm/pixel. A 100× montage of 12 frames was captured in a selected region in the middle of the sample. The 100× montage covered an area of 5.24 × 1.31 mm, with a resolution of 0.678 μm/pixel.

Microhardness indents were placed at three positions in the 50× and 100× areas to aid in aligning the optical images. Alignment of the images was performed with IMOD software (Boulder Laboratory for 3-D Electron Microscopy of Cells, University of Colorado, Boulder, CO 80309),[32] using the center of the indents in each layer for registration. The indents were replaced approximately every five layers to allow two indents at each position on a transition layer. This semiautomated alignment method produced well-registered images and no additional alignment was required. Following alignment, these indents were digitally removed to prevent them from being misidentified as voids. Micrometer measurements were used to determine cumulative removal, while individual section depth removal was checked using microhardness indent depth measurements. After 80 sections, it was determined that ~400 μm were removed, resulting in an average removal between section planes of 5 μm. The assumption of uniform removal per section eliminated cumulative measurement errors from each layer. The variation in the material removal per section was approximately 0.5 μm. Since the sample is never removed from its fixture, the parallelism between slices is defined by the parallelism between the polisher's sample holder and platen, and this was within the uncertainty from indent-derived depth measurements. Therefore, errors in void volume measurements are mainly due to dimensional uncertainty in z, which is on the order of half of the sampling depth, or 2.5 μm. IDL software (ITT Visual Information Solutions, Boulder, CO 80301)[33] was used for image segmentation, 3-D reconstruction, and feature quantification from the aligned, serially sectioned data. Voids were segmented by appropriate thresholding of the gray-scale images. The extracted voids were then stacked into a 3-D data set.

Scans completed with EBSD were collected on chemically polished (pre-etched) surfaces in order to capture spatially specific orientation data. The scan region approximately incorporated the 100× montage area, and EBSD maps were collected every 5 serial sections.
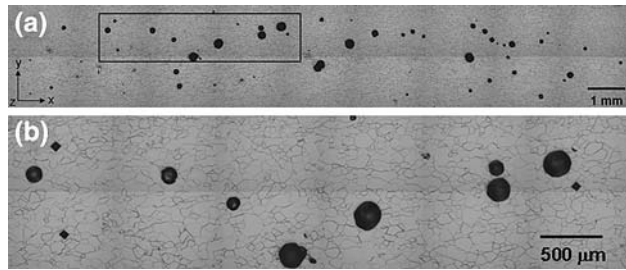

Fig. 2—Light optical micrograph montages of representative 2-D cross sections of the incipiently spalled sample incorporated in the 3-D reconstructions: (*a*) 50× overview of damage field and (*b*) 100× region corresponding to area characterized by ESBD.

As with the optical microscope images, EBSD scans were obtained at two length scales: a 2.5-μm step size for the complete 100× montage area, and 0.5- to 1-μm step sizes at select areas of interest within the 100× montage area. Data collection through EBSD was performed with OIM software and hardware (TSL-EDAX, Mahwah, NJ 07430) on a Philips XL30 FEG SEM (FEI, Hillsboro, Oregon 97124).

III. RESULTS AND DISCUSSION

A. *3-D Reconstruction and Damage Statistics*

Representative light optical montages from a cross section of the shocked tantalum target are shown in Figure 2. In the 50× overview montage (Figure 2(a)), the overall damage field appears to be composed of disconnected cavitation voids that nucleate and grow independently due to the tensile hydrostatic pressure resulting from the intersection of tensile plastic release waves at the midplane of the sample. The formation of new voids will affect the propagating shock field by creating additional surfaces that give rise to ancillary tensile release waves. The outlined area demarcates the location of the 100× montage shown in Figure 2(b), which is also in the approximate location of the EBSD scans. However, this 2-D representation cannot provide a thorough understanding of the true nature of the relationships between damage features. Figure 3(a) displays a visualization of the segmented voids reconstructed from 78 serial sections. It is important to note the significant scale of this reconstructed volume, from which 113 voids are fully contained, with an additional 96 partial voids. A region from this full set is displayed in Figure 3(b). A wide distribution of void sizes and spatial clustering are qualitatively apparent from both the 2-D and 3-D images. Quantitative statistics generated from volumetric data were subsequently calculated from this full 3-D data set.

One of the potential advantages of acquiring 3-D information is to provide a more accurate quantification of the features of interest, in this case, shock-induced damage and especially cavitation voids. To begin with, void size and shape distributions were analyzed from the 3-D data set. A histogram of the void size distribution for the 113 fully contained voids is plotted in the form of an equivalent spherical diameter in Figure 4. Accounting

for the decreased resolution in z, the voids were approximately spherical. Uncertainty in void volumes, and related equivalent diameters, is greater for smaller voids, since the fractional uncertainty in z is much greater for voids contained in relatively few sections. The
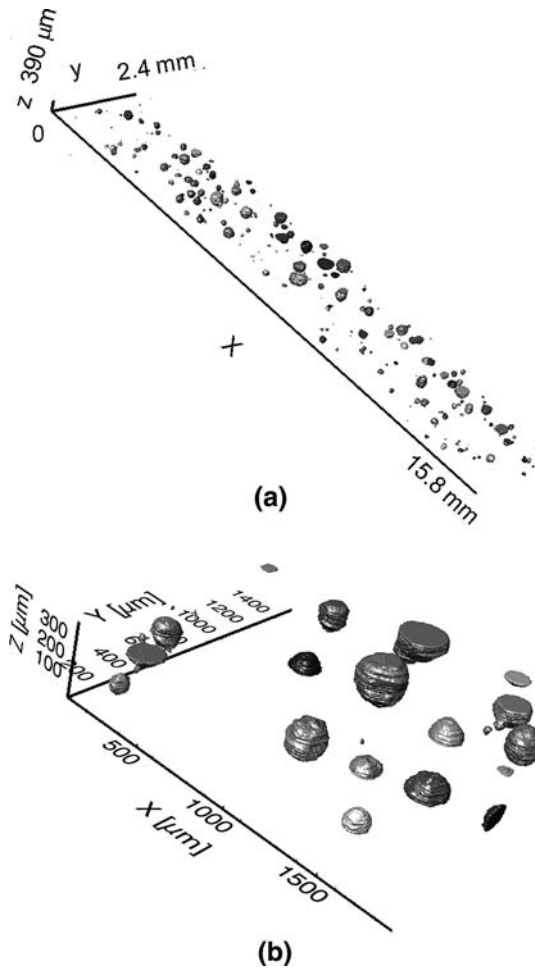

(a)

(b)

Fig. 3—3-D reconstruction of voids in damage field showing (*a*) complete damage field and (*b*) magnified view of selected region.
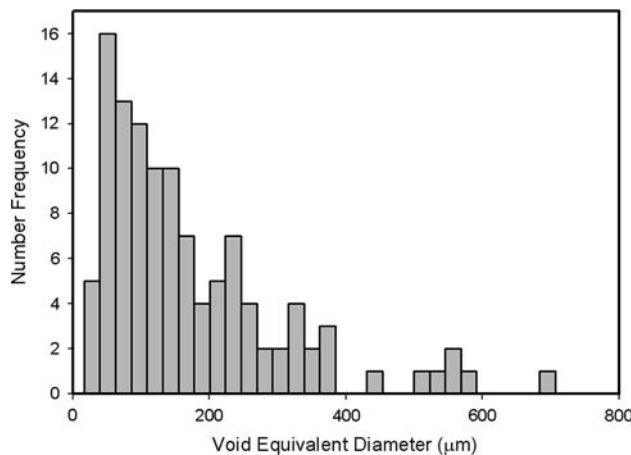

Fig. 4—Histogram of void equivalent diameter computed from 3-D volume measurements for all 113 fully contained voids in characterized volume.

mean void diameter was 172 μm, with a standard deviation (SD) of 135 μm, the median was 133 μm, and the mode 68 μm. The wide distribution of void sizes suggests either a distribution of local mean tensile stresses, a temporal distribution related to the void nucleation process, or an effect of the local surroundings, either the matrix or neighboring voids, on cavitation growth. A statistical bias will exist in the size distribution, due to the greater likelihood of large voids being partial voids, and therefore not included in the sampling. However, the sample volume incorporated virtually the entire damage field in the xy plane, so partial voids were primarily truncated along z.

Figure 5 shows a plot of orthogonal void dimensions in the x and y directions for the 113 complete voids. Analysis of the dimensional data shows that 55 pct of the voids are aspected in the x direction. Linear regression results provide a slope of 1.03 (with unity corresponding to circular cross sections) and a squared correlation coefficient (r^2) of 0.91, indicating a very weak morphological anisotropy. Figure 5 also suggests that the anisotropic effect may be greater at small strains, while voids tend to become more isotropic in the xy plane as they grow. The texture of the tantalum plate was characterized in the baseline as-received condition by EBSD, in order to investigate the potential effect of plastic anisotropy on aspherical void growth. Figure 6 shows an EBSD crystal direction map composed of a montage of scans across the through-thickness direction, y. Note the rotation in reference frame from the 2-D and 3-D section planes. The montage reveals moderate microstructural heterogeneity in the through-thickness direction. A mild texture gradient ranging from near $<001>//$ND near the surface to $<111>//$ND banding near the centerline is observed, along with some $<111>$ banding near the surfaces. The general tendency of
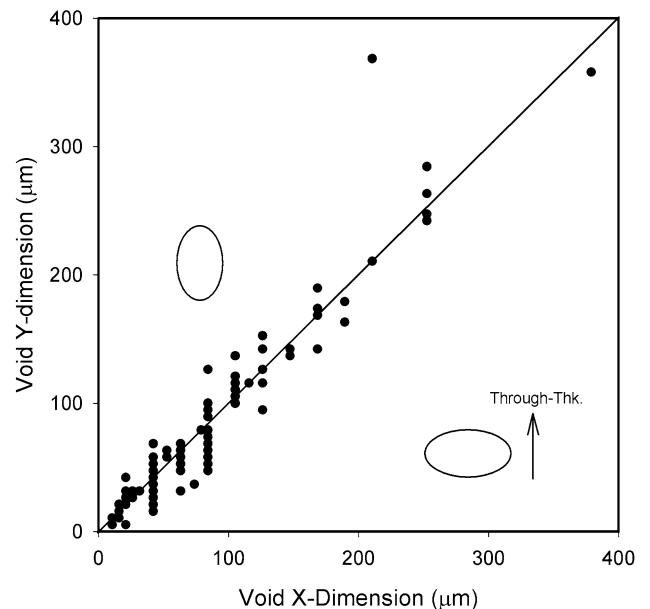

Fig. 5—Scatter plot of void dimensions in xy plane. The diagonal line represents circular cross sections; points lying below the line will be aspected along x, while those above the line will be stretched along y, the original plate through-thickness direction.

Fig. 6—Montage of EBSD crystal direction maps across thickness direction (*y*) of tantalum plate. Map color denoting crystal direction is with respect to *y*.

near-surface <001> and center-line <111> components has been previously observed in tantalum plate; in this case, it is not nearly as severe as that reported by Wright *et al.*[29] Since <111> is a plastically hard direction with respect to normal stresses in body-centered cubic metals, the <111>//ND texture near the spall plane would be expected to influence morphologic anisotropy by producing ellipsoids with *y*-direction major axes less frequently than *x*-direction major axes, as weakly observed.

Another method of quantifying void damage is to record the fraction porosity as a function of position in the *xy* plane. Figure 7 shows such a graph using data from the 3-D reconstruction, along with bounds from the constituent 2-D sections associated with the maximum and minimum total porosity. As expected for plate-on-plate spall samples, a gradient in damage exists in the *y*-direction away from the spall plane,[2] which is located at the midplane of the sample for the current geometry. However, this plot also conveys the substantial variation in measured damage as a function of sectioning position, or *z* location, as shown by the disparity between the 2-D bounds. Void size statistics from a single section may deviate substantially as a function of position, and averaged values may also incorporate significant uncertainty compared to the true 3-D values. Therefore, 2-D data should be used only with caution when describing and comparing void statistics.

An additional indication of the large variance in damage statistics as a function of section depth is the distribution of nearest-neighbor distances (NNDs).

Intervoid distance is defined here as the distance between the geometric centroids of each void. Figure 8 shows a histogram of NNDs computed from the 3-D reconstruction *vs.* those summed from four evenly spaced 2-D sections (section numbers 10, 30, 50, and 70). It is evident that 2-D section statistics tend to broaden the NND data in both the short and long directions. A schematic of three voids and their visualization within a 2-D section plane and its parent 3-D volume, as depicted in Figure 9, helps to explain this tendency. Consider voids *1* and *2* identified on a 2-D section plane in Figure 9(a), the 2-D NND of which is L_{12}^{2D}. In the true 3-D representation shown in Figure 9(b), the actual NND between 1 and 2 is L_{12}^{2D}, and this will be $\geq L_{12}^{2D}$. However, another void (*3*) that lies completely outside of the section plane, and is therefore inaccessible to the 2-D data set, may exist at a true NND of L_{13}^{3D}. In the schematic, the relative NNDs are $L_{13}^{3D} < L_{12}^{2D} < L_{12}^{3D}$. Therefore, in general, the true 3-D NND will be greater than the measured 2-D NND, unless a closer neighbor exists outside of the 2-D section plane. Since the likelihood of a closer neighbor is reduced for smaller L_{12}^{2D}, the 3-D NND data truncates small NND values by replacing them with larger true L_{12}^{3D} values. For longer L_{12}^{2D}, the probability of finding a nearer neighbor outside of the section plane increases, so the 3-D NND data also truncates the long end of the 2-D distribution. In fact, if voids are assumed to be spherical, the 2-D measurement represents the minimum possible centroid-to-centroid distance. The L_{ij}^{2D} and L_{ij}^{3D} would be equal only for the case in which the voids are
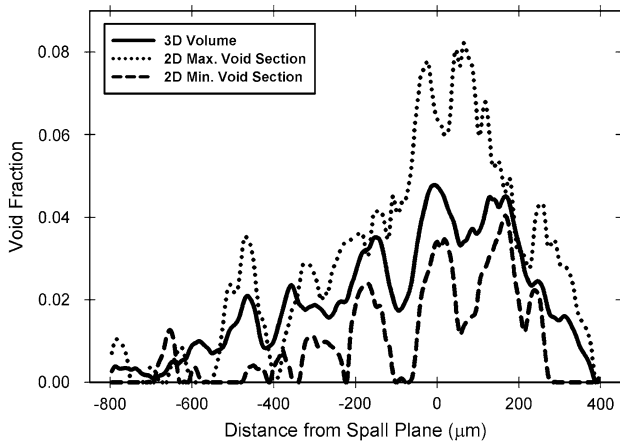

Fig. 7—Graph of spatial distribution of void damage, as measured by distance from spall plane, for the 3-D reconstructed volume along with the minimum and maximum total void fraction from the constituent 2-D sections.
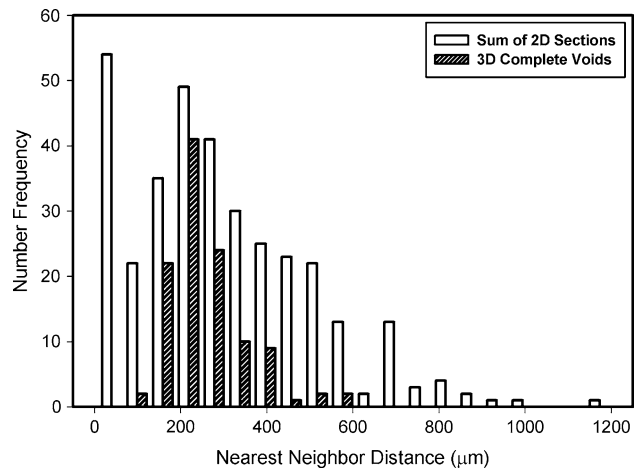

Fig. 8—Histogram of NNDs for completely contained voids in both the 3-D data set and the sum of four equally spaced 2-D sections.
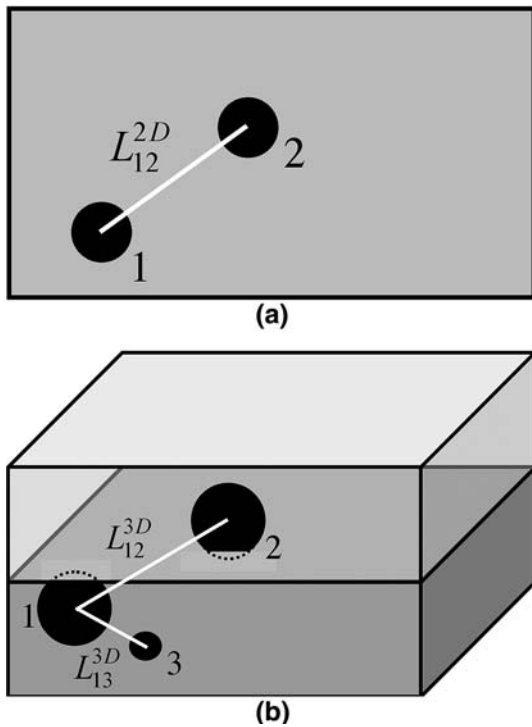
Fig. 9—Conceptual schematic illustrating measurement of neighbor distances for three voids from (*a*) a 2-D section and (*b*) the actual 3-D volume. See text for label definitions.

Fig. 10—Log-log scatter plot of void volume as a function of nearest-neighbor volume. Symbol partitions refer to grouping of relative NNDs.

of equivalent dimensions, with one of their tangential surfaces coplanar with the section plane. The average void NND, obtained from 69 complete voids, the nearest neighbors of which were also complete voids, was 220 μm with an SD of 87 μm. Including edge voids as potential nearest neighbors for all 113 complete voids (but not including edge voids the nearest neighbors of which are complete voids), the average NND was 225 μm with a SD of 95 μm. However, the NND averaged from the four 2-D sections (341 total counts) was 297 μm, with a SD of 211 μm. This clearly shows the inadequacy of 2-D data, even from several independent sections, to quantify true interfeature distances. The situation may be exacerbated in the case of preferentially oriented features. If void sites were distributed randomly throughout the damage field, the average NND would be on the order of 1 mm. The damage gradient that naturally exists as a function of distance from the spall plane complicates any interpretation, but the integrated data suggest that void site clustering exists beyond that which can be attributed to the tensile pressure decay away from the spall plane.

Several investigations[1,2,5–7] have reported that the grain-boundary (GB) network provides a preferred initiation site for void nucleation. This network includes grain boundaries, grain edges (triple points), and grain corners (vertices). It is impossible to positively identify the initiation site for larger voids; however, no smaller voids were located inconsistent with a GB network initiation site. Since the grain size of the tantalum was
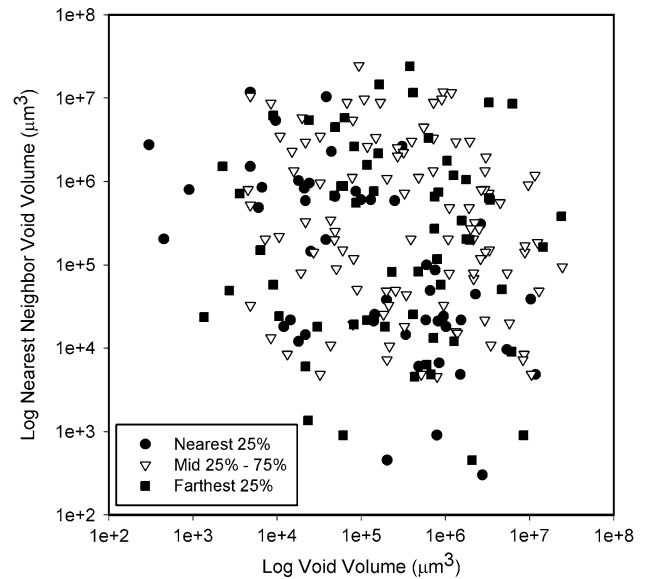
approximately 42 μm, it is clear from the average NND of 220 μm that only a subset of boundary-related preferred initiation sites for void nucleation were exploited. The nucleation of a void may result in the relaxation of local stresses that inhibits further void formation. In addition, complex interactions of the primary release wave with those emanating from the new void surfaces may relax and otherwise alter the local mean tensile stress. Figure 10 shows a scatter plot of void volume as a function of nearest-neighbor void volume for all 113 complete voids. Void pairs are segregated into the closest 25 pct, the middle 50 pct, and the farthest 25 pct neighbors. Overall, no size correlation between a void and its neighbor appears to exist. However, for the closest 25 pct nearest neighbors, there is a weak trend ($r^2 = 0.35$) toward a negative correlation, indicating that unlike sizes tend to be spatially correlated. The other two size groupings showed no correlation tendency ($r^2 < 0.02$). This lack of correlation is meaningful for the farthest neighbors, which would be expected to be correlated by large-large neighbor pairings. Overall, the size/neighbor correlation results suggest one of two possibilities: (1) the growth of a void suppresses the growth or delays the nucleation of its neighbor within a certain range (< 85 μm, in this case) or (2) the stress state surrounding a large void or associated with its inertia during growth encourages new void nucleation near it.

B. *3-D EBSD Analysis*

Characterization by EBSD was used to determine the extent of the plastic zone associated with individual voids and the void network as a whole. Figure 11 shows two intervoid regions in the form of image-quality (IQ) maps. The IQ parameter is derived from the intensity of
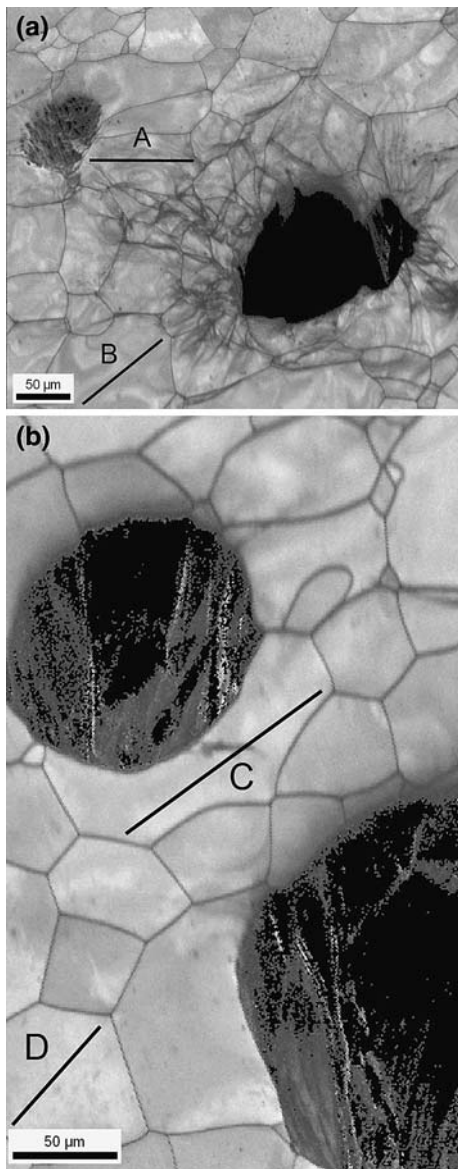
Fig. 11—EBSD-generated image-quality maps of neighboring void regions: (*a*) with substantial intervoid linkage, and (*b*) with minimal intervoid linkage. Lines marked "A" through "D" refer to locations of misorientation line scans plotted in Fig. 12.

Fig. 12—Point-to-origin misorientation line scans from indicated regions in image-quality maps (Fig. 11).

the backscattered diffraction bands, with lower IQ values correlated with greater lattice distortion. Although the IQ value is a also a function of orientation and surface quality, among other factors, regions with lower IQs (darker) have on average undergone greater deformation and resultant lattice distortion than regions of higher IQ. Thus, the IQ map provides a qualitative measure of the spatial distribution of stored work. The misorientation scans corresponding to the lines indicated in the IQ maps (Figure 11) are shown in Figure 12. This clearly indicates the range of potential misorientation development, and effective linkage, between neighboring voids. In the case of Figure 11(a), large misorientations have evolved between the voids, ranging to 15 deg along the grain containing line "A."
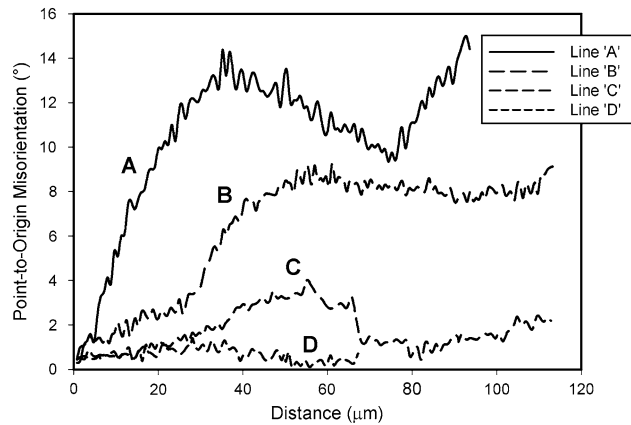
Closer to the larger void, strains were large enough in the direction of the neighboring voids to result in deformation-induced grain refinement. For the case of the voids in Figure 11(b), only moderate misorientations have evolved between voids (line "C"), although these voids are much more closely spaced than the pair in Figure 11(a). This visibly shows that spatial position is not the sole, nor possibly the most important, determinant of the probability of plastic localization and void linkage development. Away from the intervoid bridge (line "D"), and only a grain away from the larger void, misorientations are barely above annealed background levels. The plastic zone surrounding many of the voids, as measured by misorientation analyses, appears to be constrained to approximately 1 to 2 radii. The plastic zone surrounding a dynamically induced void in a viscoplastic solid has been estimated at 5 to 6 radii beyond an individual void.[34] For many of the voids, especially those that are relatively isolated, it does not appear that any appreciable plasticity occurs beyond 2 radii in the tantalum under investigation. This may be due to the constitutive properties of tantalum in the shock prestrained condition into which the voids grow.

Another method for measuring the spatial distribution of relative deformation in the microstructure is mapping the intragranular misorientation deviation (IMD). The IMD is determined for each grain by computing the average of the deviations between each discrete orientation within a grain to the grain average orientation. The grain average orientation is computed by quaternion averaging within the OIM software analysis package. Grains in this case were defined by a 15-deg misorientation criterion. A comparison of the IQ map and an IMD map for the identical 2-D region is shown in Figures 13(a) and (b), respectively. Regions of lower IQ are directly associated with larger IMD values. The vast majority of these strain-related features are undetected by light optical metallography. The IMD maps reinforce the observations from the misorientation line scans (Figures 11 and 12); independent voids, or linked voids in directions away from the linkage propagation, display very limited plastically affected zones. Some of the high-IMD zones are located in
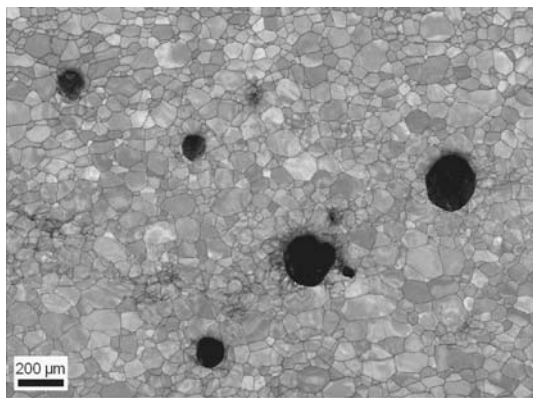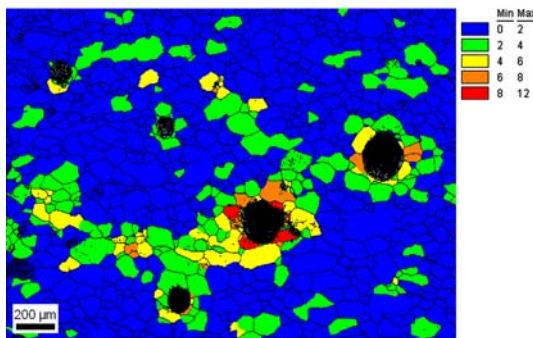
Fig. 13—EBSD-generated maps from region containing multiple voids: (*a*) image-quality map and (*b*) IMD map from identical region. Scale in (*b*) refers to IMD number in degrees.

Fig. 14—IMD map of representative region of as-received tantalum plate. The vast majority of grains lie below the 2-deg threshold.

regions that do not display voids on the 2-D section plane. In order to determine whether these linked IMD regions are associated with an interconnected void network in the out-of-plane dimension, a 3-D reconstruction of IMD maps was performed.

Regions of approximately 4.6 mm in the radial direction by 1.7 mm in the through-thickness directions, contained within the 100× montage area, were analyzed to produce 2-D IMD maps. A lower-limit IMD of 2 deg was applied, below which grains were considered undeformed. This threshold was selected after an analysis of as-annealed tantalum from the identical plate as the shocked sample. Since the deformation level of the as-annealed material is essentially nil, any IMD would be due to experimental error or subgrain misorientations, the latter of which were not a factor in this material. Dislocation content in the spall sample may be increased relatively uniformly throughout the microstructure, due to the passage of the plastic shock wave. However, deviatoric strains enable void linkage, and these strains result in the plastic spin that produces larger IMDs. The IMD for a representative section of as-annealed material is shown in Figure 14. Only a few grains, representing 3 pct of the total area, exhibit an IMD > 2 deg. For comparison, using a 1-deg threshold, approximately 7 pct of the area, was selected. Therefore, a 2-deg threshold was deemed to be selective enough in the spalled m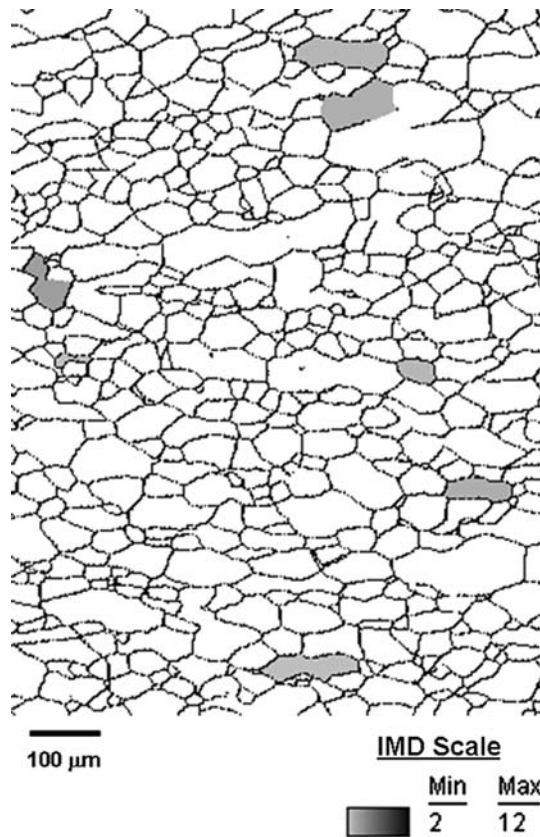aterial to eliminate the overwhelming majority of nondeviatorically strained grains, yet at a low enough level to capture even modest levels of deformation. The IMD maps were thus computed for each EBSD-measured section, and then reconstructed in 3-D. Contiguous grains above the defined threshold were uniquely colored, and voids on the upper section were rendered black. The 3-D IMD reconstruction, therefore, shows different linkage scales of plastically deformed grains along the spall plane, as defined by selected IMD thresholds.

Figure 15(a) shows the 3-D IMD reconstructed volume at a 2-deg threshold. A continuous intervoid linkage network exists across the volume, indicating a very broad and diffuse incipient spall plane. This may be intensified by the shock prestrain deformation in addition to shear linkage processes. The IMD volumes with 3- and 4-deg thresholds are shown in Figures 15(b) and (c), respectively. At a 3-deg threshold, the IMD network is becoming discontinuous, with islands of material deformed to this limit surrounding individual voids. A larger contiguous region can still be identified. Using a 4-deg threshold further isolates 'deformed' regions, yet a large contiguous region still exists, and in fact persists to a 7-deg threshold. This region may represent a shear localization precursor. The higher threshold reveals a more localized and topologically planar feature than the broad expanse of linkage suggested at 2 deg. The planarity is consistent with the evolving development of a spall failure surface. Longer pulse durations or greater peak pressures may have been required to
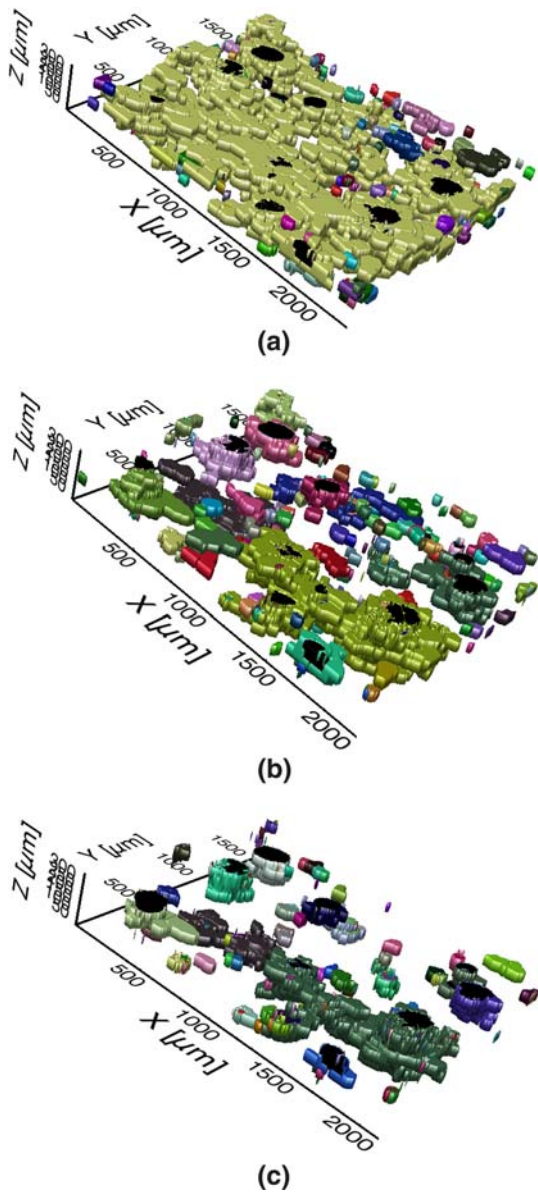
Fig. 15—3-D reconstruction of IMD maps from selected volume of spall sample. Unique color indicates contiguously linked grains that have IMD values above the following thresholds: (*a*) 2, (*b*) 3, and (*c*) 4 deg. Black areas at surface designate void locations.

produce more intense strain localization and eventual fracture. It should be noted that the detection of this connectivity is only accessible to 3-D characterization, and that using IQ mapping, for instance, does not reveal the extent of the deformation-affected zone.

In contrast to the sample examined in this study, equivalent tantalum material shocked with longer pulse durations clearly exhibits mixed-mode damage, with prominent regions of shear localization linking many voids.[3] The question remains whether the later-stage mixed-mode damage develops from: (1) two temporally distinct regimes consisting of void nucleation and growth until a threshold mean intervoid distance is reached, followed by plastic instability between preexisting voids and percolative linkage or (2) the contem-

poraneous evolution of void nucleation and growth with shear linkage. The initial shear linkages in the latter process would perhaps provide preferred nucleation sites for subsequent void formation. The former situation would suggest that the shorter duration sample examined in this study had already reached a critical void density, since incipient shear linkage zones were identified. In either case, this may imply that shorter duration conditions represent an intermediate damage structure on a path to the mixed-mode damage observed at longer durations. Furthermore, if this is the case, then the initial plasticity field as observed in this study provides a template for subsequent intense localizations, and/or additional void nucleation regions, that eventually produce spall failure surfaces.

IV. CONCLUSIONS

A 3-D microstructural reconstruction from an incipiently spalled tantalum sample provided true quantitative information regarding the damage network. It was found that the mean and median void spherical equivalent diameters were 172 and 133 μm, respectively. The texture and texture heterogeneity did not appear to exert a strong influence on void shape in the case of tantalum. The average NND was 220 μm, while correlations between the void size and the NND were only evident for the 25 pct closest neighbors, which exhibited a positive correlation between unlike sizes. The equivalent statistics from individual 2-D sections indicate significant variances that highlight the inadequacy of nonvolumetric data sources to elicit true damage and microstructural quantitative data. The EBSD analysis highlighted the relatively short characteristic distances of the damage field surrounding individual cavitation voids, and the heterogeneity of intervoid ligament structures. The IMD mapping, however, revealed regions of contiguous void linkage. Reconstructions of these IMD maps in three dimensions illustrated regions of connectivity that may be precursors to strain localization linkages between voids, ultimately resulting in spall failure. Future efforts investigating mixed-mode damage characteristics will seek to establish the evolutionary mechanism leading to spall failure. The goal remains to determine the true nature of the damaged state, to inform and help develop more realistic material damage models.

REFERENCES

1. M.A. Meyers and C.T. Aimone: *Progr. Mater. Sci.*, 1983, vol. 28, pp. 1–96.
2. J.M. Rivas, A.K. Zurek, W.R. Thissell, D.L. Tonks, and R.S. Hixson: *Metall. Mater. Trans. A*, 2000, vol. 31A, pp. 845–51.
3. W.R. Thissell, A.K. Zurek, D.L. Tonks, and R.S. Hixson: *AIP Conf. Proc.*, Ammerican Institute of Physics, Melville, NY 11747, 2000, vol. 505, pp. 451–54.
4. W.R. Thissell, D.L. Tonks, D. Schwartz, and J. House: *AIP Conf. Proc.*, 2004, vol. 706, pp. 495–98.
5. A. Molinari and T.W. Wright: *J. Mech. Phys. Sol.*, 2005, vol. 53, pp. 1476–1504.
6. P. Chevrier and J.R. Klepaczko: *Eng. Fract. Mech.*, 1999, vol. 63, pp. 273–94.
7. R.W. Minich, J.U. Cazamias, M. Kumar, and A.J. Schwartz: *Metall. Mater. Trans. A*, 2004, vol. 35A, pp. 2663–73.
8. X. Chen, J.R. Asay, and S.K. Dwivedi: *J. Appl. Phys.*, 2006, vol. 99, pp. 023528-1–02352813.
9. R. Cortes: *Int. J. Solids Struct.*, 1992, vol. 29, pp. 1637–45.
10. G.T. Gray III and J.C. Huang: *Mater. Sci. Eng.*, 1991, vol. A145, pp. 21–35.
11. E.T. Seppala, J. Belak, and R.E. Rudd: *Phys. Rev. B*, 2004, vol. 69, pp. 134101-1–134101-19.
12. F.L. Addessio and J.N. Johnson: *J. Appl. Phys.*, 1993, vol. 74, pp. 1640–48.
13. L. Campagne, L. Daridon, and S. Ahzi: *Mech. Mater.*, 2005, vol. 37, pp. 869–86.
14. J.P. Bandstra, D.A. Koss, A.B. Geltmacher, P. Matic, and R.K. Everett: *Mater. Sci. Eng.*, 2004, vol. A366, pp. 269–81.
15. S.-R. Chen and G.T. Gray III: *Metall. Mater. Trans. A*, 1996, vol. 27A, pp. 2994–3006.
16. M.V. Kral, M.A. Mangan, G. Spanos, and R.O. Rosenberg: *Mater. Characterization*, 2000, vol. 45, pp. 17–23.
17. M.V. Kral and G. Spanos: *Acta Mater.*, 1999, vol. 47, pp. 711–24.
18. J. Alkemper and P. Voorhees: *Acta Mater.*, 2001, vol. 49, pp. 897–902.
19. A.C. Lund and P. Voorhees: *Phil. Mag.*, 2003, vol. 83, pp. 1719–33.
20. A.J. Kubis, G.J. Shiflet, D.N. Dunn, and R. Hull: *Metall. Mater. Trans. A*, 2004, vol. 35A, pp. 1935–43.
21. H. Agarwal, A.M. Gokhale, S. Graham, and M.F. Horstemeyer: *Metall. Mater. Trans.*, 2002, vol. 33A, pp. 2599–2606.
22. R.J. Larsen and B.L. Adams: *Metall. Mater. Trans. A*, 2004, vol. 35A, pp. 1991–98.
23. K.M. Dobrich, C. Rau, and C.E. Krill: *Metall. Mater. Trans.*, 2004, vol. 35A, pp. 1953–61.
24. H. Singh and A.M. Gokhale: *Mater. Characterization*, 2005, vol. 54, pp. 21–29.
25. D.M. Saylor, A. Morawiec, and G.S. Rohrer: *Acta Mater.*, 2003, vol. 51, pp. 3663–74.
26. R.K. Everett, K.E. Simmonds, and A.B. Geltmacher: *Scripta Mater.*, 2001, vol. 44, pp. 165–69.
27. L.B. Wang, J.D. Frost, G.Z. Voyiadjis, and T.P. Harman: *Mech. Mater.*, 2003, vol. 35, pp. 777–90.
28. J.J. Gammage, D.S. Wilkinson, J.D. Embury, and E. Maire: *Phil. Mag.*, 2005, vol. 85, pp. 3191–206.
29. S.I. Wright, G.T. Gray III, and A.D. Rollett: *Metall. Mater. Trans. A*, 1994, vol. 25A, pp. 1025–31.
30. M.A. Meyers: *Dynamic Behavior of Materials*, 1st ed., John Wiley & Sons, New York, NY, 1994, pp. 523–46.
31. A.M. Kelly, S.R. Bingert, and R.D. Reiswig: *Microstruct. Sci.*, 1998, vol. 23, pp. 185–95.
32. J.R. Kremer, D.N. Mastronarde, and J.R. McIntosh: *J. Struct. Biol.*, 1996, vol. 116, pp. 71–76.
33. M. Piper and M.D. Galloy: *Introduction to IDL Software*, Research Systems, Inc, Boulder, CO, 2004, pp. 1–214.
34. X.Y. Wu, K.T. Ramesh, and T.W. Wright: *J. Mech. Phys. Solids*, vol. 51, pp. 1–26.